

# Coupled Mode Theory for Semiconductor Nanowires

Robert Buschlinger,<sup>1</sup> Michael Lorke,<sup>2</sup> and Ulf Peschel<sup>1</sup>

<sup>1</sup>*Institute of Condensed Matter Theory and Optics, Abbe Center of Photonics,  
Friedrich Schiller University of Jena, Max-Wien-Platz 1, 07743 Jena, Germany*

<sup>2</sup>*Institute for Theoretical Physics, University of Bremen, 28359 Bremen, Germany*

We present a model to describe the spatiotemporal evolution of guided modes in semiconductor nanowires based on a coupled mode formalism. Light-matter interaction is modelled based on semiconductor Bloch equations, including many-particle effects in the screened Hartree-Fock approximation. Appropriate boundary conditions are used to incorporate reflections at waveguide endfacets, thus allowing for the simulation of nanowire lasing. We compute the emission characteristics and temporal dynamics of *CdS* and *ZnO* nanowire lasers and compare our results both to Finite-Difference Time-Domain simulations and to experimental data. Finally, we explore the dependence of the lasing emission on the nanowire cavity and on the materials relaxation time.

## I. INTRODUCTION

An increasing demand for fast communication technologies and the limitations inherent to electronic integrated circuits has stimulated the research on nanophotonic components. In particular semiconductor nanowires have gathered widespread interest due to their simple fabrication and their remarkable photonic properties, which allow them to act as efficient waveguides and as resonators either for photonic and plasmonic lasing or for harnessing polaritonic effects.<sup>1–5</sup>

Semiconductor nanowires are complex photonic systems supporting multiple longitudinal as well as transverse modes interacting through the nonlinear response of the medium. The optical properties of the medium are influenced by many-body effects of the excited carriers, which give rise to excitonic absorption peaks and the appearance of polaritons in the weakly excited regime. In the strongly excited regime, effects like phase-space filling, screening and excitation-induced dephasing dominate the optical response,<sup>6–9</sup> giving rise to a broad gain profile. In order to make correct predictions across the different regimes of excitation conditions, theoretical models of light-matter interaction in semiconductor nanowires need to incorporate all these effects.

Recently, we proposed a coupled Finite-Difference Time-Domain (FDTD)<sup>10,11</sup> and semiconductor Bloch equations (SBEs)<sup>8,9</sup> approach to the modelling of light-matter interaction in arbitrary semiconductor geometries<sup>12</sup>. A similar approach has also been applied to the description of semiconductor quantum wells.<sup>13</sup> While models based on the FDTD method are the most general, the numerical complexity can be decreased considerably if assumptions are made concerning the simulated geometry.

In the present case we deal with nanowires, where the propagating fields can be decomposed into waveguide eigenmodes. A considerable simplification of the numerical treatment is achieved by describing the evolution of the eigenmode amplitudes in the framework of coupled mode theory (CMT). In the general case a transverse resolution is needed, but considerably less data points than

in the case of a more general approach like FDTD are necessary. The resulting reduction in computational demands makes it possible to increase the simulated time window and the size and complexity of the nanowire geometry or to include even more sophisticated material models capturing additional effects relevant for semiconductor lasers as comprehensively summarized in<sup>14,15</sup>.

In this paper, we describe our coupled mode theory for semiconductor nanowires including the treatment of reflecting endfacets. We apply the model to the simulation of the temporal dynamics of *ZnO* nanowire-lasers and compare our results to data from an experimental study<sup>16</sup>.

## II. THEORETICAL MODEL

### A. Derivation of propagation equations

In the following, we summarize the derivation of evolution equations for the slowly varying envelopes of waveguide modes under the influence of material nonlinearities and dispersion, which have been used in similar form by other authors.<sup>17,18</sup> We start with Maxwell's equations in the frequency domain

$$\nabla \times \vec{E} = i\omega\mu_0\vec{H} \quad (1)$$

$$\nabla \times \vec{H} = -i\omega\varepsilon_0\varepsilon\vec{E} - i\omega\vec{P}. \quad (2)$$

The polarization term  $\vec{P}$  couples the material model including dispersion, absorption and nonlinearity to the equations for the electromagnetic fields. We consider a waveguide extending in the  $z$ -direction, which in the unperturbed case ( $\vec{P} = 0$ ) supports modes with the transverse field profiles  $\vec{E}_m^\pm(x, y)$ ,  $\vec{H}_m^\pm(x, y)$  and the propagation constants  $\pm\beta_m$ . Neglecting group velocity dispersion, the propagation constant close to the frequency  $\omega_0$  takes the form

$$\beta_m = \beta_{0,m} + \frac{1}{v_m}(\omega - \omega_0), \quad (3)$$

with  $\beta_{0,m} = \beta_m(\omega_0)$  and  $\frac{1}{v_m} = \left[ \frac{\partial \beta_m}{\partial \omega} \right]_{\omega_0}$  being the modes inverse group velocity at  $\omega_0$ . Note, that by using this simplification we merely neglect the group velocity dispersion arising from the frequency-dependent changes of the mode shape. Any dispersion effects caused by the resonant excitation of the semiconductor material remain unaffected.

The fields propagating in the perturbed waveguide ( $\vec{P} \neq 0$ ) can be decomposed into propagating modes as

$$\vec{E} = \sum_{\pm, m} u_m^{\pm}(z) \vec{E}_m^{\pm} \quad (4)$$

$$\vec{H} = \sum_{\pm, m} u_m^{\pm}(z) \vec{H}_m^{\pm}. \quad (5)$$

We now analyze the vector  $\vec{\Gamma}_m = \vec{E} \times \vec{H}_m^{\pm*} e^{\mp i \beta_m z} + \vec{E}_m^{\pm*} e^{\mp i \beta_m z} \times \vec{H}$ , which can be interpreted as the contribution of mode  $m$  to the Poynting vector. Using equations (1) and (2), we find that

$$\text{div } \vec{\Gamma}_m = i\omega \vec{E}_m^{\pm*} \vec{P} e^{\mp i \beta_m z}. \quad (6)$$

Next we integrate equation (6) with respect to the transverse coordinates  $x$  and  $y$ . As  $\vec{\Gamma}_m$  decays exponentially with  $x$  and  $y$  approaching infinity, we obtain

$$\begin{aligned} \int_{-\infty}^{\infty} \int_{-\infty}^{\infty} \frac{d}{dz} \left( \left[ \vec{E} \times \vec{H}_m^{\pm*} + \vec{E}_m^{\pm*} \times \vec{H} \right]_z e^{\mp i \beta_m z} \right) dx dy \\ = i\omega \int_{-\infty}^{\infty} \int_{-\infty}^{\infty} \left( \vec{E}_m^{\pm*} \vec{P} e^{\mp i \beta_m z} \right) dx dy \end{aligned} \quad (7)$$

Next, we insert the mode expansion (4),(5) into equation (7). Due to the orthogonality of the modes, we obtain the expression

$$\frac{d}{dz} u_m^{\pm} \mp i \beta_m u_m^{\pm} = \frac{i\omega}{4\gamma_m} \int_{-\infty}^{\infty} \int_{-\infty}^{\infty} \left( \vec{E}_m^{\pm*} \vec{P} \right) dx dy \quad (8)$$

using the guided power of mode  $m$  defined as

$$\gamma_m = \frac{1}{4} \int_{-\infty}^{\infty} \int_{-\infty}^{\infty} \left( \vec{E}_m^{\pm} \times \vec{H}_m^{\pm*} + \vec{E}_m^{\pm*} \times \vec{H}_m^{\pm} \right)_z dx dy. \quad (9)$$

We insert equation (3) and transform equation (8) back to the time-domain using the inverse Fourier transforms  $\vec{P}(z, t) = \mathcal{F}^{-1} \{ \vec{P} \}$  and  $u(z, t) = \mathcal{F}^{-1} \{ u \}$ . We further define slowly varying envelopes for the mode amplitudes

$$\hat{u}(z, t) = u(z, t) e^{i\omega_0 t - i\beta_0 z} \quad (10)$$

and for the polarization

$$\hat{\vec{P}}(z, t) = \vec{P}(z, t) e^{i\omega_0 t}, \quad (11)$$

and arrive at the evolution equation

$$\pm \frac{1}{v_m} \frac{\partial}{\partial t} (\hat{u}_m^{\pm}) = -\frac{d}{dz} \hat{u}_m^{\pm} + D e^{\mp i \beta_{0m} z} \quad (12)$$

for the slowly varying envelopes with the driving term

$$D = -\frac{\frac{\partial}{\partial t} - i\omega_0}{4\gamma_m} \int_{-\infty}^{\infty} \int_{-\infty}^{\infty} \left( \vec{E}_m^{\pm*} \hat{\vec{P}} \right) dx dy. \quad (13)$$

The self-consistent electric field driving the polarization used in equation (13) is given as a superposition of all modes, taking into account the individual mode shapes. For some applications it can be desirable to include a pump field  $\vec{E}_{pump}(\vec{r}, t)$ , which mainly propagates in directions perpendicular to the waveguide axis and therefore does not contribute to the guided modes directly. Thus, the self-consistent field is described as

$$\begin{aligned} \vec{E}(\vec{r}, t) = \sum_{\pm, m} \hat{u}_m^{\pm}(z, t) \vec{E}_m^{\pm}(x, y) e^{\pm i \beta_0 z} e^{-i\omega_0 t} \\ + \vec{E}_{pump}(x, y, z, t). \end{aligned} \quad (14)$$

## B. Material Model

To complete the description of the system, the polarization  $\vec{P}$  has to be modelled by a separate evolution equation governed by the material system. We use the model published in Ref.<sup>12</sup>, which we shortly summarize here. Our model uses a semiconductor Bloch equations<sup>8,9</sup> approach including many-particle effects in the Screened Hartree-Fock approximation and is adapted to 2-6 semiconductors.<sup>12</sup> The microscopic polarizations  $\psi_{\lambda, q, k}$  as well as the occupation numbers  $n_{s, k}$  for conduction-band electrons ( $s = e$ ) and for holes in the different valence bands ( $s = \lambda$ ) are assumed to depend only on the absolute value  $k$  of the Bloch vector  $\vec{k}$ . Then, the complex polarization in a bulk semiconductor takes the form

$$\vec{P} = \sum_{\lambda, q} \int_0^{\infty} dk \frac{k^2}{\pi^2} \vec{d}_{\lambda, q, k} \psi_{\lambda, q, k}, \quad (15)$$

where  $\vec{d}_{\lambda, q, k}$  is the dipole matrix element attributed to the transition from valence band  $\lambda$  to the conduction band and coupling to the electric field component pointing in direction  $q$ . The evolution of the microscopic polarizations is described by<sup>8,9</sup>

$$\begin{aligned} i\hbar \frac{\partial}{\partial t} \psi_{\lambda, q, k} = (1 - n_{e, k} - n_{\lambda, k}) \Omega_{\lambda, q, k} \\ + (\varepsilon_{e, k} + \varepsilon_{\lambda, k} + \varepsilon_{\lambda, gap} - \Delta \varepsilon_k - i\gamma(N)) \psi_{\lambda, q, k} + \Gamma_{\psi, \lambda, q, k}, \end{aligned} \quad (16)$$

Parameter	Description	Value <i>CdS</i>	Value <i>ZnO</i>
$\varepsilon_{gap,a}$	Gap energy valence band a	2420meV	3372meV
$\varepsilon_{gap,b}$	Gap energy valence band b	2435meV	3382meV
$\varepsilon_{gap,c}$	Gap energy valence band c	-	3416meV
$m_{eff,e}$	Effective mass electrons	0,1619 $m_e$	0,28 $m_e$
$m_{eff,a}$	Effective mass valence band a	0,5951 $m_e$	0,59 $m_e$
$m_{eff,b}$	Effective mass valence band b	0,713 $m_e$	0,59 $m_e$
$m_{eff,c}$	Effective mass valence band c	-	0,45 $m_e$
$n_{bg}$	Background refractive index	2.81	2.0
$d_0$	Dipole matrix element	0.279e · nm	0.42e · nm
$\gamma(N)$	Polarization dephasing rate	5ps <sup>-1</sup> + 4 × 10 <sup>-5</sup> $\frac{cm}{ps}$ N <sup>0.3</sup>	30ps <sup>-1</sup> + 2 × 10 <sup>-5</sup> $\frac{cm}{ps}$ N <sup>0.3</sup>
$\gamma_{rec}$	Carrier recombination rate	10 <sup>9</sup> s <sup>-1</sup>	10 <sup>9</sup> s <sup>-1</sup>
$\gamma_{f,e}$	Intraband relaxation rate e <sup>-</sup>	10 <sup>12</sup> s <sup>-1</sup>	2 × 10 <sup>12</sup> s <sup>-1</sup>
$\gamma_{f,h}$	Intraband relaxation rate holes	10 <sup>13</sup> s <sup>-1</sup>	2 × 10 <sup>12</sup> s <sup>-1</sup>
$\gamma_{ba}$	Rel. rate valence band b to a	6 × 10 <sup>9</sup> s <sup>-1</sup>	6 × 10 <sup>9</sup> s <sup>-1</sup>
$\gamma_{ca}$	Rel. rate valence band c to a	-	1 × 10 <sup>12</sup> s <sup>-1</sup>

Table I: Material parameters as used in the semiconductor Bloch equations models for *ZnO* and *CdS*.

where  $\Omega_{\lambda,q,k}$  are renormalized Rabi-frequencies

$$\Omega_{\lambda,q,k} = \vec{d}_{\lambda,q,k} \vec{E} + \int_0^\infty dk' W_{k,k'} \psi_{\lambda,q,k'}. \quad (17)$$

The transition energies are given by the sum of the renormalized single-particle energies

$$\varepsilon_{s,k} = \frac{\hbar^2 k^2}{2m_{eff,s}} - \int_0^\infty dk' W_{k,k'} n_{s,k'}, \quad (18)$$

of species  $s$  and the band gap of each transition  $\varepsilon_{\lambda,gap}$ . In order to correctly describe the highly excited semiconductor, the renormalized Rabi-frequencies and transition-energies are calculated using the screened Coulomb matrix-elements  $W_{k,k'}$  instead of the unscreened matrix elements  $V_{k,k'}$ .<sup>9,12</sup> Therefore the inclusion of the Coulomb-hole contribution

$$\Delta\varepsilon_k = \int_0^\infty dk' (W_{k,k'} - V_{k,k'}) \quad (19)$$

is necessary.<sup>8</sup> Finally,  $\gamma(N)$  describes the excitation-density dependent damping of the polarization<sup>12,19,20</sup> and  $\Gamma_{\psi,\lambda,q,k}$  represents a noise term driving spontaneous emission.<sup>21,22</sup>

The time evolution of the occupation numbers is given by

$$\begin{aligned} \frac{\partial}{\partial t} n_{e,k} = & -\frac{2}{\hbar} \sum_{\lambda,q} \Im (\Omega_{\lambda,q,k} \psi_{\lambda,q,k}^*) - \gamma_{rec} \sum_{\lambda} n_{\lambda,k} n_{e,k} \\ & + \gamma_{f,e} (f_{e,k} - n_{e,k}) + \Gamma_{n_{e,k}} \end{aligned} \quad (20)$$

for electrons and by

$$\begin{aligned} \frac{\partial}{\partial t} n_{\lambda,k} = & -\frac{2}{\hbar} \sum_q \Im (\Omega_{\lambda,q,k} \psi_{\lambda,q,k}^*) - \gamma_{rec} n_{\lambda,k} n_{e,k} \\ & + \gamma_{f,h} (f_{\lambda,k} - n_{\lambda,k}) + \sum_{\lambda' \neq \lambda} \Delta_{\lambda\lambda'k} + \Gamma_{n_{\lambda,k}}. \end{aligned} \quad (21)$$

for holes in the valence band  $\lambda$ . The first term describes the carrier excitation by the electromagnetic field. The two terms involving  $\gamma_{rec}$  and  $\gamma_f$  respectively describe non-radiative recombination and intra-band relaxation of carriers towards Fermi-Dirac distributions with a band dependent fermi level  $f_{s,k}$ .<sup>23</sup> To allow for the relaxation between valence bands, an additional contribution  $\sum_{\lambda' \neq \lambda} \Delta_{\lambda\lambda'k}$  is included in the equation of motion for the hole populations, with

$$\Delta_{\lambda\lambda'k} = \gamma_{\lambda'\lambda} n_{\lambda',k} (1 - n_{\lambda,k}) - \gamma_{\lambda\lambda'} n_{\lambda,k} (1 - n_{\lambda',k}). \quad (22)$$

Similar as in the case of the polarization, noise terms  $\Gamma_{n_{e,k}}$  and  $\Gamma_{n_{\lambda,k}}$  are added to the evolution equations for the electron and hole occupation numbers.

2-6 semiconductors are uniaxial crystals with the optical axis or  $c$ -axis pointing along the wire in  $z$ -direction. Optical transitions occur between a single  $s$ -like conduction band (occupation number  $n_{e,k}$ ) and three valence bands (occupation numbers  $n_{\lambda,k}$ ,  $\lambda \in \{a, b, c\}$ ).<sup>24,25</sup> Assuming conservation of electron spin, allowed transitions are characterized by a conservation of angular momenta of photons and electrons. From this, we obtain the transitions  $\psi_{a/b/c,x/y,k}$ , coupling to fields polarized in the  $x/y$ -direction perpendicularly to the crystals  $c$ -axis and the transitions  $\psi_{b/c,z,k}$  coupling to the fields polarized in  $z$ -direction pointing along the  $c$ -axis.<sup>12,24,25</sup>

The model parameters used in this publication are summarized in table I. For the verification of the model

in section III, we compare CMT and FDTD simulations of an optically pumped *CdS* nanowire laser. In accordance with the FDTD code developed in<sup>12</sup> we neglect any coupling to valence band *c*, since the excitation is assumed to be close to the fundamental band gap. In contrast, the third valence band is included for the simulations of *ZnO*-nanowire lasers presented in section IV, since the excitation frequency lies above the respective band gap.

### C. Numerical Considerations

Equation (12) is discretized on an equally spaced grid in both time and propagation length

$$[\hat{u}_m^\pm]_j^i = \hat{u}_m^\pm(i\Delta z, j\Delta t)$$

using central finite differences with temporal and spatial discretization steps correlated as

$$\Delta t = \frac{\Delta z}{|v|}. \quad (23)$$

Only for this choice numerical instabilities can be avoided. We obtain the discretized propagation equations

$$\begin{aligned} [\hat{u}_m^+]_{j+1}^{i+1} &= [\hat{u}_m^+]_j^i + \frac{\Delta t}{2} D_{j+\frac{1}{2}}^{i+\frac{1}{2}}, \\ [\hat{u}_m^-]_{j+1}^{i-1} &= [\hat{u}_m^-]_j^i + \frac{\Delta t}{2} D_{j+\frac{1}{2}}^{i-\frac{1}{2}}. \end{aligned} \quad (24)$$

If a material polarization as described in section II B is discretized using central finite differences, the driving terms  $D$  have to be evaluated on temporally staggered timesteps  $j + \frac{1}{2}$ . As an approximation to the values required for an exact evaluation of equation (24), which are also staggered in space, we use  $D_{j+\frac{1}{2}}^{i\pm\frac{1}{2}} \approx D_{j+\frac{1}{2}}^i$ .

The transverse integral over the waveguide cross-section in equation (13) can be evaluated using a spatial discretization scheme appropriate for the waveguide geometry. Usually the transverse resolution can be kept low, using only few data points. For instance we use a resolution of 4 radial steps and 16 azimuthal steps for our simulations of a single-mode waveguide with a radius of  $r = 80nm$  presented below.

Especially for the simulation of lasing nanowires, where the interference between forward and backward propagating waves is strong and intensities vary on the scale of  $\frac{\lambda}{2n}$ , we have to chose a fine longitudinal discretization for the determination of the material response given by  $D$ . Due to the stability criterion (23), this resolution requirement also determines the temporal resolution. The material equations however are not subject to this stability criterion, since they merely have to resolve the highest frequencies present in the slowly varying envelopes. Since in our case the computational demands are mainly determined by the solution of the material equations, we

can further reduce the time needed for computation by restricting the number of timesteps at which the SBEs are evaluated. This can be accomplished by skipping every  $N_{skip}$  timesteps in the evaluation of the SBEs and using linear interpolation whenever values from intermediate steps are required. In our lasing example, we can restrict the evaluation of the material equations to every  $N_{skip} = 6$ th step. However this number is determined by the detuning between material resonance and envelope center frequency and by the shape of the envelope signals themselves and could be higher or lower depending on the simulated scenario.

The field evolution inside the nanowire laser is heavily influenced by boundary conditions, which we will discuss next. Reflecting boundaries like the endfacets of a nanowire laser cavity can be implemented by inserting the appropriate amplitudes propagating away from the interface. Assuming that equation (14) is evaluated on points with spatial indices  $i \in [0, N_z - 1]$ , general expressions for the two missing amplitudes at the boundaries are

$$[\hat{u}_m^-]_j^{N_z} = \sum_n R_{mn} [\hat{u}_n^+]_j^{N_z-1} \quad (25)$$

$$[\hat{u}_m^+]_j^{-1} = \sum_n R_{mn} [\hat{u}_n^-]_j^0 \quad (26)$$

The reflectivity matrix elements<sup>26</sup>  $R_{mn}$  as well as the mode profiles  $\vec{E}_m^\pm(x, y)$ ,  $\vec{H}_m^\pm(x, y)$  and the pump field  $\vec{E}_{pump}(\vec{r}, t)$  have to be determined beforehand by analytical estimates or with numerical tools like FDTD using the nondispersive and linear background refractive index of the nanowire material. In the unperturbed propagation equations ( $D = 0$ ), the prescribed reflectivities are the only source of reflection from the endfacets. If the mode amplitudes are coupled to the material equations, there exists an additional contribution to the reflectivity which is caused by the missing material polarization outside the simulation volume. While the prescribed reflectivities describe the reflection at the endfacet of a nanowire with the materials background index  $n_{bg}$ , this contribution accounts for the reflectivity caused by the electronic part of the refractive index.

### III. VERIFICATION

To verify our method, we compare it to direct simulations of light propagation in semiconductor nanowires using the coupled FDTD and semiconductor Bloch equations approach.<sup>12</sup>

Due to the initial exponential growth in intensity and the strength of nonlinear effects, nanowire lasers constitute an extremely demanding test case for our model. We now consider a highly excited *CdS* ( $n_{bg} = 2.81$ ) nanowire laser with length  $l = 8\mu m$  and radius  $r = 80nm$ . At a central wavelength of  $\lambda = 512nm$ , the wire only supports the two degenerate fundamental modes as shown in the

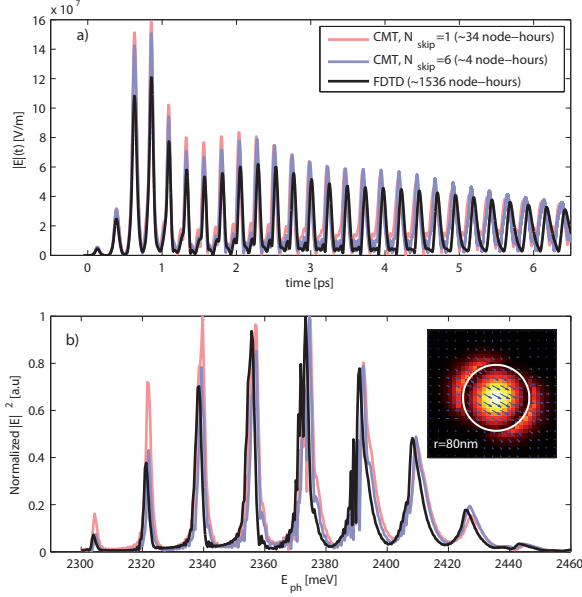


Figure 1: Temporal evolution (a) and lasing spectrum (b) of a  $CdS$  nanowire laser with radius  $r = 80nm$  and length  $l = 8\mu m$  surrounded by air at initial quasiparticle densities of  $N_{el} = 3 \times 10^{19} cm^{-3}$ ,  $N_{h,a} = N_{h,b} = 1.5 \times 10^{19} cm^{-3}$  calculated using the FDTD method (black curve) and the CMT method using both evaluation of the material equations at each timestep (red curves) and at each 6th timestep (blue curves). The wire supports only the doubly degenerate fundamental mode. The intensity profile (colour) and field direction (arrows) as used in the FDTD simulation is shown in the insert of panel (b). The mode is not completely rotationally symmetric, but shows lobes outside the nanowire in polarisation direction. The mode profile used by the CMT code is generated by interpolation of this profile onto a coarse cylindrical coordinate system with 4 radial and 16 angular points.

inset of Fig. 1(b)), propagating with group velocity  $v_g = 7.72 \times 10^7 \frac{m}{s}$  and propagation constant  $\beta_0 = 22.28 \frac{1}{\mu m}$ . To create a laser cavity, the wire is terminated by realistic endfacets with an amplitude reflectivity matrix as used in equations (25) and (26)

$$R = \begin{pmatrix} 0.51 & 0.02 \\ 0.02 & 0.51 \end{pmatrix} \quad (27)$$

extracted from a simple linear FDTD simulation of a wire endfacet<sup>26</sup>. The occupation probabilities for electrons and holes are initialized with Fermi-distributions at  $T = 300K$  for spatial densities of  $N_{el} = 3 \times 10^{19} cm^{-3}$ ,  $N_{h,a} = N_{h,b} = 1.5 \times 10^{19} cm^{-3}$ . In order to avoid a randomization of the lasing output which would render direct comparisons between the two codes difficult, we switch off spontaneous emission and instead start the laser with a sech-shaped seed pulse with a pulse duration of  $w_t = 20fs$ . The spatial resolution in the FDTD simulation is  $\Delta x = \Delta y = \Delta z = 10nm$ . In the CMT simulation we use a longitudinal resolution of  $\Delta z = 10nm$ ,

while the transverse fields are sampled using a cylindrical coordinate system with  $N_R = 4$  radial steps. Due to the high mode confinement, the modal fields have a significant longitudinal contribution, which is not radially symmetric. Therefore, also an azimuthal resolution with  $N_\theta = 16$  steps is necessary in order to achieve good agreement with FDTD simulations. We use both simulations where the material equations are solved on the same temporal grid as the propagation equations ( $N_{skip} = 1$ ) and on a grid with  $N_{skip} = 6$ . In this special case the simulation becomes unstable, if we try to further reduce the temporal resolution of the material equations. However the CMT variety with  $N_{skip} = 6$  already is approximately 400 times as fast as the FDTD method.

Fig. 1(a) shows the time-resolved electrical field strength recorded at one endfacet of the nanowire. Since the seed pulse is amplified and reflected inside the cavity, a train of pulses is emitted at the endfacet. We initially observe a fast rise in lasing intensity. After the inversion in the spectral region of the main longitudinal mode has been depleted, the emission switches to other longitudinal modes with lower gain, leading to a slow decay in the lasing intensity similar to the results in<sup>12</sup>. Despite the dramatically reduced computation time, the CMT results show excellent agreement with the FDTD results concerning the spectral position of the lasing modes (Fig. 1(b)). The temporal dynamics (Fig. 1(a)) also show good qualitative agreement concerning the shape of the emitted pulse train as well as the position of the individual pulses, which is directly linked to the modal dispersion under the influence of the material system. However, the overall intensity of the emitted pulse train is higher in the CMT simulation. Near-perfect agreement can be achieved by tuning of the endfacet reflectivity used by the CMT code. From this we conclude, that the difference in emission intensity is caused by the imperfect modelling of the endfacet reflectivity under the influence of the material system, which is an inherent limitation of Coupled Mode Theory. However, the endfacet reflectivities of real nanowires will always vary due to imperfections in growth and preparation, giving rise to fluctuations of laser performance in experiments. Most importantly, the essential laser dynamics are already captured very well by our model.

#### IV. TEMPORAL DYNAMICS OF NANOWIRE LASERS

Since the increased efficiency of the presented model allows us to simulate the entire excitation and lasing process in a comparatively short time, it is now possible to perform a more comprehensive analysis of the properties of semiconductor nanowire lasers. In our further analysis, we choose  $ZnO$  wires ( $n_{bg} = 2.0$ ) due to the wealth of available experimental data<sup>16,27,28</sup> for this material system. We specifically model our nanowires after experiments performed by Wille et al.<sup>16</sup>, where time-

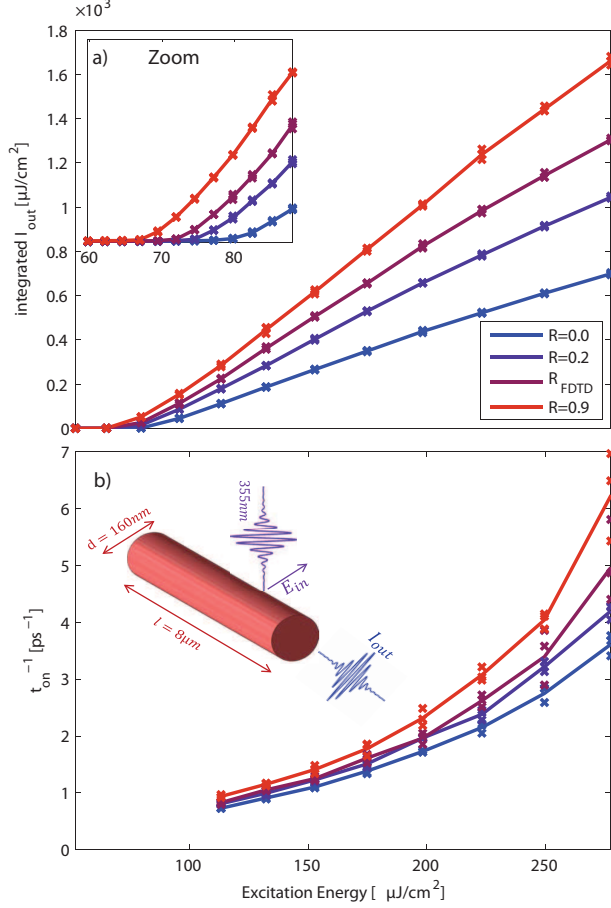


Figure 2: Emission properties of exemplary *ZnO*-nanowire lasers with different endfacet reflectivities (a): Output energy for different pump energies, the inset shows a zoom into the region around the laser-threshold. (b): Inverse emission onset time for different pump energies in the lasing regime. The results from individual runs with different random number seeds for the spontaneous emission noise are shown by markers. The lineplots show the averaged data for each nanowire configuration.

resolved  $\mu$ -PL measurements have been used in order to investigate the temporal dynamics of the lasing emission. An important parameter extracted from the experiment is the emission onset time  $t_{on}$ , which is defined as the time between the maximum of the pump pulse and the buildup of the laser emission to  $\frac{1}{e}$  of its maximum. In the lasing regime, the inverse emission onset time  $t_{on}^{-1}$  is reported to increase nonlinearly with increasing pump power. Additionally, time-resolved spectra have been obtained from the experiment and a spectral red-shift of the lasing modes occurring during emission has been observed. This has been attributed to the depletion of excited carriers due to stimulated emission, which leads to an increase of the refractive index and therefore to a shift in the energies of the wires longitudinal Fabry-Perot modes.

While the main goal of our simulations is the reproduction of the experimental features outlined above, we

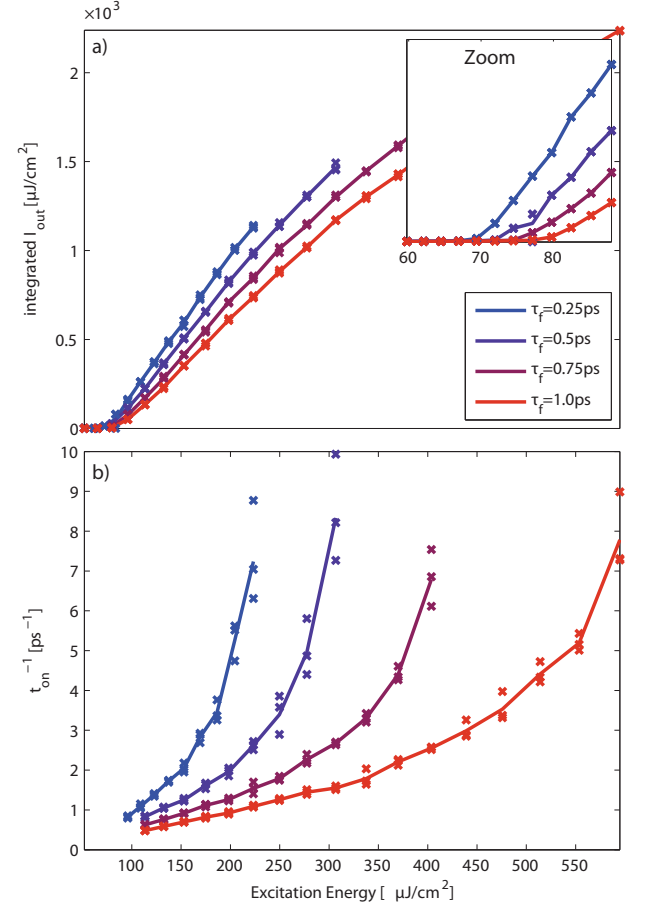


Figure 3: Emission properties of exemplary *ZnO*-nanowire lasers with different intraband relaxation times  $\tau_f = \frac{1}{\gamma_f}$  (a): Output energy for different pump energies. (b): Inverse emission onset time for different pump energies in the lasing regime. The solid lines show data averaged over three runs with different random seeds (crosses).

are additionally going to investigate the dependence of the laser emission on parameters which can vary from sample to sample and are not easily accessible in experiments. We study exemplary nanowires with a length  $l = 8\mu m$  and a diameter of  $d = 160nm$  as sketched in the inset of Fig. 2(b). Since the wire diameter is definitely in the single-mode regime, we restrict our simulations to the fundamental *HE*01 mode with a propagation constant  $\beta_0 = 24.32 \frac{1}{\mu m}$  and group velocity  $v_g = 1.26 \times 10^8 \frac{m}{s}$ . The diagonal endfacet reflectivity  $R_{m,m} = 0.29$  extracted from FDTD simulations is slightly lower than for the *CdS*-wire. To decrease simulation time, we restrict the transverse resolution to a single point. This will not exactly reproduce results as they would be obtained by an FDTD-simulation, but allows us to capture the essential physics in the present case of a single-mode wire. The wires are optically pumped from above with sech-shaped pulses with a temporal width of  $w_t = 2ps$  and a central wavelength of  $\lambda = 355nm$ , polarized perpendicularly to

the wire axis. The exciting field is assumed to be homogeneous along the wire. Since the output can vary from realization to realization due to different random seed values for the spontaneous emission noise in equations (16), (20) and (21), we average over several simulation runs. As the fluctuations are not excessively strong, the averaging procedure is restricted to three runs.

First, we investigate the emission properties of several wires with varying endfacet reflectivity in the range between the extreme values  $R = 0.0$  and  $R = 0.9$  and including the reflectivity  $R_{FDTD}$  as extracted from FDTD simulations. The endfacet reflectivity of real nanowires can vary strongly between different samples and strongly affects the quality of the optical cavity. Note, that simulations with a nominal endfacet reflectivity of  $R = 0.0$  still have a finite reflectivity due to the material boundary effect described in section II C. The input/output curves resulting from our simulations are given in Fig. 2(a) and show the typical lasing behaviour which exhibits a linear increase above a certain threshold intensity of approximately  $W_{th} = 70 \mu J/cm^2$ . The laser threshold power lies below the experimental value of  $W_{th} = 200 \mu J/cm^2$ , but is of the same order of magnitude. This is to be expected, since we prescribe a homogeneous electric field inside the wire and do not take into account effects like scattering of the exciting waves from the wire or a spatially inhomogeneous excitation. As expected, wires with lower endfacet reflectivities achieve a lower efficiency. Fig. 2(b) shows the inverse emission onset time  $t_{on}^{-1}$ . As reported in the experiment, lasing generally sets in faster with increasing excitation power. We also observe an increase of  $t_{on}^{-1}$  for higher endfacet reflectivities. Since our model does not include an excitation-dependent carrier relaxation time, this increase can be explained solely by the fact that the laser threshold is reached at an earlier time, if a stronger pump pulse is used. The same effect occurs, if we lower the lasing threshold by increasing the endfacet reflectivity (see inset of Fig. 2(a)). Additionally, roundtrip losses are lowered in this case, allowing for a faster buildup of lasing oscillations.

After having investigated the influence of the optical cavity by simulating wires with different endfacet reflectivities, we now consider the influence of the semiconductor relaxation dynamics, which are governed by the intraband relaxation time  $\tau_f = \frac{1}{\gamma_f}$ .

Fig. 3(a) shows simulated input/output curves for different values of  $\tau_f$ . We observe a decreasing lasing efficiency for increasing intraband relaxation times. This is due to the fact, that the lasing process is slowed down for high relaxation times. Thus, a higher number of carriers can recombine by the way of other relaxation processes before being used for spontaneous emission. As expected, the slowed down dynamics also leads to a strong decrease in the inverse emission onset time  $t_{on}^{-1}$  (3(b)). However, the nonlinear increase of  $t_{on}^{-1}$  with increasing pump power is retained for all simulated values of  $\tau_f$ .

Finally, we use a windowed Fourier-transform in order to obtain the time-resolved lasing spectrum (Fig. 4(b))

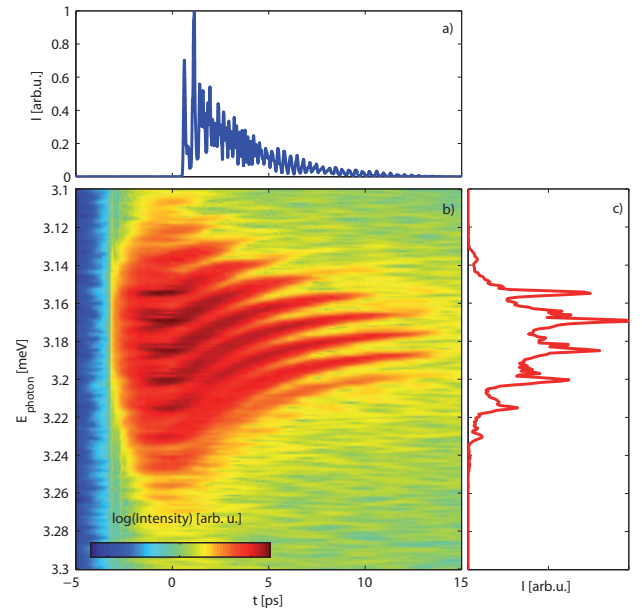


Figure 4: (a): Temporal intensity profile of lasing output from an exemplary *ZnO* nanowire. (b): Dynamics of the individual lasing modes obtained from a windowed Fourier-transform of the temporal data. (c): Spectral intensity of the laser emission obtained from a Fourier-transform over the whole output pulse duration. All data has been averaged over three simulation runs with different random number input for the spontaneous emission.

of one of our wire configurations with  $R = R_{FDTD}$  and  $\tau_f = 0.5 ps$ , which produces similar temporal dynamics as measured in the experiment.<sup>16</sup>

The temporal lasing profile and the time-averaged spectrum are given in (Fig. 4) (a) and (c), respectively. Similar to the experiment, we observe a pronounced red-shift of the lasing modes during the emission process due to the change in the materials refractive index caused by the depletion of quasi-particles.

## V. CONCLUSION

In conclusion, we have developed a new theoretical model for the simulation of light-matter interaction and lasing in semiconductor nanowire structures based on the framework of coupled mode theory coupled to semiconductor Bloch equations. We have shown that our model can qualitatively and quantitatively reproduce the results achieved by a more general FDTD model, but with a speedup of up to three orders of magnitude depending on the simulated setup and the required accuracy. We have further applied the model to the simulation of the properties and temporal dynamics of *ZnO*-nanowire lasers. We reproduce the red-shift of the lasing modes occurring during the emission process as well as the nonlinear increase of the inverse emission onset time with increasing excitation power, which have been observed in



experiments<sup>16</sup>. Further, we have studied the influence of the optical cavity as well as the carrier relaxation time on the laser dynamics. We observe a reduction of the emission onset time both with increasing endfacet reflectivity and with decreasing material relaxation time. In the future, the computational efficiency of our model is going to pave the way for the inclusion of more advanced material models as well as more complicated geometries in full time-domain simulations of semiconductor nanowires.

## Acknowledgments

The authors gratefully acknowledge financial support by Deutsche Forschungsgemeinschaft (Forschergruppe FOR1616, projects P5 and E4). The authors thank Robert Röder and Marcel Wille for helpful discussions.

- <sup>1</sup> X. Duan, Y. Huang, R. Agarwal, and C. M. Lieber, *Nature* **421**, 241 (2003), URL <http://dx.doi.org/10.1038/nature01353>.
- <sup>2</sup> R. F. Oulton, V. J. Sorger, T. Zentgraf, R.-M. Ma, C. Gladden, L. Dai, G. Bartal, and X. Zhang, *Nature* **461**, 629 (2009), URL <http://dx.doi.org/10.1038/nature08364>.
- <sup>3</sup> T. P. H. Sidiropoulos, R. Röder, S. Geburt, O. Hess, S. A. Maier, C. Ronning, and R. F. Oulton, *Nat Phys* **advance online publication** (2014), ISSN 1745-2481, URL <http://dx.doi.org/10.1038/nphys310310.1038/nphys3103><http://www.nature.com/nphys/journal/vaop/ncurrent/abs/nphys3103.html#supplementary-information>.
- <sup>4</sup> D. Saxena, S. Mookapati, P. Parkinson, N. Jiang, Q. Gao, H. H. Tan, and C. Jagadish, *Nature Photonics* **7**, 963 (2013), URL <http://dx.doi.org/10.1038/nphoton.2013.303>.
- <sup>5</sup> R. Röder, M. Wille, S. Geburt, J. Rensberg, M. Zhang, J. G. Lu, F. Capasso, R. Buschlinger, U. Peschel, and C. Ronning, *Nano Letters* **13**, 3602 (2013), <http://pubs.acs.org/doi/pdf/10.1021/nl401355b>, URL <http://pubs.acs.org/doi/abs/10.1021/nl401355b>.
- <sup>6</sup> K. ElSayed, L. Bányai, and H. Haug, *Phys. Rev. B* **50**, 1541 (1994).
- <sup>7</sup> G. Manzke and K. Henneberger, *phys. stat. sol. (b)* **234**, 233 (2002).
- <sup>8</sup> W. Chow and S. Koch, *Semiconductor-Laser Fundamentals: Physics of the Gain Materials* (Springer, 1999), ISBN 9783540641667, URL <http://books.google.de/books?id=ltEAFxGT3pgC>.
- <sup>9</sup> H. Haug and S. Koch, *Quantum Theory of the Optical and Electronic Properties of Semiconductors (4th Edition)* (World Scientific, 2004), ISBN 9789812387561, URL <http://books.google.de/books?id=-UoG0Hx0w04C>.
- <sup>10</sup> K. S. Yee, *IEEE Trans. Antennas and Propagation* pp. 302–307 (1966).
- <sup>11</sup> A. Taflov and S. C. Hagness, *Computational Electrodynamics: The Finite-Difference Time-Domain Method, Third Edition* (Artech House, 2005), 3rd ed., ISBN 1580538320, URL <http://www.worldcat.org/isbn/1580538320>.
- <sup>12</sup> R. Buschlinger, M. Lorke, and U. Peschel, *Phys. Rev. B* **91**, 045203 (2015), URL <http://link.aps.org/doi/10.1103/PhysRevB.91.045203>.
- <sup>13</sup> S. Guazzotti, A. Pusch, D. E. Reiter, and O. Hess, *Phys. Rev. B* **94**, 115303 (2016), URL <http://link.aps.org/doi/10.1103/PhysRevB.94.115303>.
- <sup>14</sup> K. Böhringer and O. Hess, *Progress in Quantum Electronics* **32**, 159 (2008), ISSN 0079-6727, URL <http://www.sciencedirect.com/science/article/pii/S0079672708000220>.
- <sup>15</sup> K. Böhringer and O. Hess, *Progress in Quantum Electronics* **32**, 247 (2008), ISSN 0079-6727, URL <http://www.sciencedirect.com/science/article/pii/S0079672708000232>.
- <sup>16</sup> M. Wille, C. Sturm, T. Michalsky, R. Röder, C. Ronning, R. Schmidt-Grund, and M. Grundmann, *Nanotechnology* **27**, 225702 (2016), URL <http://stacks.iop.org/0957-4484/27/i=22/a=225702>.
- <sup>17</sup> B. Crosignani, P. D. Porto, and C. H. Papas, *Opt. Lett.* **6**, 61 (1981), URL <http://ol.osa.org/abstract.cfm?URI=ol-6-2-61>.
- <sup>18</sup> A. Snyder and J. Love, *Optical Waveguide Theory*, Science paperbacks (Springer, 1983), ISBN 9780412099502, URL [http://books.google.co.in/books?id=gIQB\\\_hzB0SMC](http://books.google.co.in/books?id=gIQB\_hzB0SMC).
- <sup>19</sup> W. Hügel, M. Heinrich, and M. Wegener, *physica status solidi (b)* **473**, 473 (2000), URL [http://onlinelibrary.wiley.com/doi/10.1002/1521-3951\(200009\)221:1%3C473::AID-PSSB473%3E3.0.CO;2-I/abstract](http://onlinelibrary.wiley.com/doi/10.1002/1521-3951(200009)221:1%3C473::AID-PSSB473%3E3.0.CO;2-I/abstract).
- <sup>20</sup> H. Haug, *physica status solidi (b)* **221**, 179 (2000), ISSN 1521-3951, URL [http://dx.doi.org/10.1002/1521-3951\(200009\)221:1<179::AID-PSSB179>3.0.CO;2-6](http://dx.doi.org/10.1002/1521-3951(200009)221:1<179::AID-PSSB179>3.0.CO;2-6).
- <sup>21</sup> J. Andreasen and H. Cao, *J. Lightwave Technol.* **27**, 4530 (2009), URL <http://jlt.osa.org/abstract.cfm?URI=jlt-27-20-4530>.
- <sup>22</sup> J. Andreasen and H. Cao, *Phys. Rev. A* **82**, 063835 (2010), URL <http://link.aps.org/doi/10.1103/PhysRevA.82.063835>.
- <sup>23</sup> Y. Huang and S.-T. Ho, *Opt. Express* **14**, 3569 (2006), URL <http://www.opticsexpress.org/abstract.cfm?URI=oe-14-8-3569>.
- <sup>24</sup> D. G. Thomas and J. J. Hopfield, *Phys. Rev.* **116**, 573 (1959), URL <http://link.aps.org/doi/10.1103/PhysRev.116.573>.
- <sup>25</sup> D. G. Thomas and J. J. Hopfield, *Phys. Rev.* **128**, 2135 (1962), URL <http://link.aps.org/doi/10.1103/PhysRev.128.2135>.
- <sup>26</sup> A. V. Maslov and C. Z. Ning, *Applied Physics Letters* **83**, 1237 (2003), URL <http://scitation.aip.org/content/aip/journal/apl/83/6/10.1063/1.1599037>.
- <sup>27</sup> R. Röder, T. P. H. Sidiropoulos, C. Tessarek, S. Christiansen, R. F. Oulton, and C. Ronning, *Nano Letters* **15**, 4637 (2015), pMID: 26086355, <http://dx.doi.org/10.1021/acs.nanolett.5b01271>, URL <http://dx.doi.org/10.1021/acs.nanolett.5b01271>.
- <sup>28</sup> R. Röder, T. P. H. Sidiropoulos, R. Buschlinger, M. Riediger, U. Peschel, R. F. Oulton, and C. Ronning, *Nano Letters* **0**, null (0), pMID: 27007261,



<http://dx.doi.org/10.1021/acs.nanolett.6b00811>, URL  
<http://dx.doi.org/10.1021/acs.nanolett.6b00811>.